Lawrence Berkeley National Laboratory

Lawrence Berkeley National Laboratory

Title

Synthesis and Electrochemical Characterization of M2Mn3O8 (M=Ca, Cu) Compounds and Derivatives

Permalink

https://escholarship.org/uc/item/15q0j8ww

Authors

Park, Yong Joon
Doeff, Marca M.

Publication Date

2005-08-25

eScholarship.org Powered by the California Digital Library
University of California

Synthesis and Electrochemical Characterization of $M_2Mn_3O_8$ (M=Ca, Cu) Compounds and Derivatives

Yong Joon Park[1,2] and Marca M. Doeff[1]

1) Materials Sciences Division

Lawrence Berkeley National Laboratory

University of California

Berkeley, CA 94720 USA

and

2) Power Source Device Team, Electronics and Telecommunications Research Institute

161 Gajeong-dong, Yuseong-gu, Daejeon, 305-350, KOREA

Acknowledgment

This work was supported by the Assistant Secretary for Energy Efficiency and Renewable Energy, Office of FreedomCAR and Vehicle Technologies of the U.S. Department of Energy under contract no. DE-AC02-05CH11231. This work was also supported by the Korea Research Foundation Grant (M01-2004-000-20008-0) (YJP). We would like to thank Dr. Kwang Sun Ryu for helpful discussion.

Abstract

$M_2Mn_3O_8$ ($M=Ca^{2+}$, Cu^{2+}) compounds were synthesized and characterized in lithium cells. The M^{2+} cations, which reside in the van der Waal's gaps between adjacent sheets of $Mn_3O_8^{4-}$, may be replaced chemically (by ion-exchange) or electrochemically with Li. More than 7 $Li^+/Cu_2Mn_3O_8$ may be inserted electrochemically, with concomitant reduction of Cu^{2+} to Cu metal, but less Li can be inserted into $Ca_2Mn_3O_8$. In the case of Cu^{2+}, this process is partially reversible when the cell is charged above 3.5 V *vs.* Li, but intercalation of Cu^+ rather than Cu^{2+} and Li^+/Cu^+ exchange occurs during the subsequent discharge. If the cell potential is kept below 3.4 V, the Li in excess of $4Li^+/Cu_2Mn_3O_8$ can be cycled reversibly. The unusual mobility of +2 cations in a layered structure has important implications both for the design of cathodes for Li batteries and for new systems that could be based on M^{2+} intercalation compounds.

Keywords: manganese oxides, lithium battery cathodes, divalent cations

Introduction

Layered manganese oxides are of interest as cathode materials for lithium batteries due to the potential for very high energy densities. In actuality, the electrochemical properties of these materials are very dependent upon the stacking arrangements, the nature and amount of any substituents, [1] and the presence or absence of vacancies in the transition metal layers [2, 3]. In this context, the family of manganese oxides having the general formula $M_2Mn_3O_8$, where M is a +2 cation such as Co [4], Mn, Cd [5], Zn [6], Cu [7], or Ca [8] is of considerable interest. These structures are generally composed of infinite $Mn_3O_8^{4-}$ sheets between which the +2 ions are located. The $Mn_3O_8^{4-}$ sheets resemble the MnO_2 layers in O3 structures such as α-$NaMnO_2$ [9], being comprised of a double layer of oxygen in a cubic close-packed array, with octahedral sites for manganese. These are completely filled for α-$NaMnO_2$, but only ¾ filled with Mn in $M_2Mn_3O_8$ in such a way as to produce ordered vacancies (Figure 1a). An alternative notation for the $Mn_3O_8^{4-}$ sheets, therefore, is $Mn_{3/4}O_2^{-}$ and, in the ideal structure, all of the Mn is in the +4 oxidation state, in contrast to α-$NaMnO_2$ where all of the Mn is +3. The coordination of the divalent cations located between the manganese oxide sheets varies depending upon the metal. For example, Cu^{2+}, which is a Jahn-Teller ion, is displaced towards the transition metal vacancies, resulting in square pyramidal coordination (Figure 1b), whereas large Ca^{2+} ions have trigonal prismatic coordination (Figure 1c). In both cases, there are unfilled interlayer sites; e.g., one with tetrahedral symmetry and one with octahedral, adjacent to each Ca^{2+} ion in $Ca_2Mn_3O_8$. The empty 2d and interlayer sites provide possible locations for Li^{+} ions intercalated during

discharge of $M_2Mn_3O_8$ electrodes in lithium cells, although insertion of Li^+ into the latter would most likely require rearrangement of the divalent cations due to their proximity.

Both Cu^{2+} and Mn^{4+} ions in $Cu_2Mn_3O_8$ can be expected to show redox activity in the potential range where manganese oxides normally discharge, leading potentially to a very high energy density system. The behavior may resemble that of the recently described $Cu_{2.33}V_4O_{11}$ system, in which both Cu and V undergo reduction [10] during cell discharge. In contrast, the Ca^{2+} in $Ca_2Mn_3O_8$ should be electrochemically inactive, so that only Mn undergoes reduction. A comparison of the two systems should allow the various redox processes occurring during discharge of $Cu_2Mn_3O_8$ to be identified unequivocally.

Somewhat surprisingly, our results indicate that, in both the $Ca_2Mn_3O_8$ and $Cu_2Mn_3O_8$ systems, the divalent cations are completely displaced from the structure upon intercalation of lithium, implying that they are highly mobile. The ultimate product in both cases is a new lithiated manganese oxide phase with a layered structure, which is also redox active; in effect, this is an electrochemically driven ion-exchange. A related, but not structurally identical, phase can also be produced chemically, by reaction of $Ca_2Mn_3O_8$ with molten lithium nitrate, as described below.

Experimental

$Ca_2Mn_3O_8$ was prepared by a sol-gel method from $Mn(CH_3CO_2)_2{\cdot}4H_2O$ and $Ca(NO_3)_2{\cdot}4H_2O$. The starting materials were dissolved in distilled water and glycolic acid was mixed into the solution so that the molar ratio of glycolic acid to metal ions was 2: 1. Ammonium hydroxide was then added to increase the pH to about 9~10. The solution was then heated to 80^{o}C until it formed a viscous pink gel. The gel was fired at 450^{o}C for 5 hours during which time a vigorous decomposition process occurred resulting in an

ash-like powder. The decomposed powder was ground and heated to 750°C for 5 hours under a flow of O_2 gas.

$Cu_2Mn_3O_8$ was prepared by a modification of a previously reported hydrothermal method [11]. $KMnO_4$, $Mn(NO_3)_2{\cdot}4H_2O$ and CuO were mixed together so that the molar ratios of KMnO4: $Mn(NO_3)_2{\cdot}4H_2O$ were 2:3 and that of CuO:Mn was 1:1, respectively. This mixture was introduced into a Parr bomb and water was added in the proportion of $4H_2O$ per mole of Mn. The bomb was sealed and heated to 170 °C for 12 hours. It was then opened and the contents were homogenized. A solution of $Cu(NO_3)_2{\cdot}3H_2O$ saturated at 20°C was added in the proportion of 400 cc/mole of manganese. The bomb was sealed again and heated to 250°C for 13 days. The products of reaction were $Cu_2(OH)_3NO_3$, CuO, and $Cu_2Mn_3O_8$. Washing thoroughly with sulfuric acid allowed the pure $Cu_2Mn_3O_8$ phase to be isolated.

A lithiated product was also prepared by the reaction of $Ca_2Mn_3O_8$ with molten lithium nitrate. $Ca_2Mn_3O_8$ was heated in a 20-fold excess of molten $LiNO_3$ at 350°C for 48 hours. The resultant brown powder was washed with distilled water and the process was repeated. After a final washing with distilled water, the product was dried at 130°C for 24h. The surface area of this powder was determined by BET (Brunauer-Emmett-Teller) analysis using a surface area and porosity analyzer (Micromeritics, Tristar).

Elemental analyses (ICP) were carried out by Desert Analytics (Tucson, AZ). Products were identified by x-ray powder diffraction, using a Philips X'Pert diffractometer in the 2θ range from 10 to 70° with monochromatized Cu-Kα radiation. Unit cell parameters were determined by fitting patterns with PowderCell 2.4 (W. Kraus and G. Nolze). Redox titrations [12] were carried out to determine the oxidation state of

Mn in the samples. A 0.1-g portion of sample was initially dissolved in an excess of aqueous solution of $FeSO_4(NH_4)_2(SO_4)\bullet H_2O$ (0.03 mol/L), in the presence of H_2SO_4 and H_3PO_4. All the Mn^{n+} ions were thus reduced into Mn^{2+} by the ferrous ions. The excess Fe^{2+} ions were subsequently titrated by an acidic solution (H_2SO_4) of $K_2Cr_2O_7$ (0.005 mol/L), using sodium diphenylamine sulfonate indicator (1% in acidic solution).

For the preparation of positive electrodes, 0.5 g of polyvinyl difluoride (PVdF, Kynar) was dissolved in about 7 g of N-methyl-2-pyrrolidone for 1 hour and then 3.5 g of sample powder, 0.5 g of carbon black and 0.5 g of SFG-6 graphite (Timrex Timcal) were added. After 3 hours of mixing, the resultant viscous slurry was coated on an aluminum foil using a doctor blade and dried at 100^{o}C in a vacuum oven. Electrochemical cells were assembled in a dry box from positive electrodes cut out from the coated foils, lithium metal, Celgard 3401 separators, and 1M $LiPF_6$ solution in 2:1 ethylene carbonate/dimethyl carbonate (v:v, Merck). Cells were subjected to galvanostatic and potentiostatic cycling using a MacPile II(Bio-Logic,SA, Claix, France) or an Arbin BT/HSP-2043 cycler.

Results and Discussion

Synthesis and Structure

Figure 2 shows the calculated diffraction pattern for $Ca_2Mn_3O_8$ and that obtained for the powder prepared by sol-gel. The pattern was indexed assuming a space group of C2/m and the unit cell parameters listed in Table 1; these were essentially identical to those in a previous report [8]. The peaks are somewhat broad due to the small particle size; BET analysis indicated a surface area of 50-55 M^2/g for this material.

Attempts to synthesize $Cu_2Mn_3O_8$ via sol-gel and glycine-nitrate combustion methods failed, resulting in multi-phase mixtures. Above 500°C, $Cu_2Mn_3O_8$ decomposes to form a Cu-containing spinel [11], severely limiting the possibilities for solid-state synthesis. A modified version of a hydrothermal method previously reported in reference 11 was used successfully to generate nearly phase-pure $Cu_2Mn_3O_8$; however, for reaction times less than 13 days under the conditions used, a significant birnessite-like impurity was observed in all the samples. The XRD pattern for a sample of phase-pure $Cu_2Mn_3O_8$ is presented in Figure 3. The sharp reflections indicate that this material is highly crystalline. The calculated pattern is also shown, assuming the space group C2/m and the lattice parameters listed in Table 1; in this case, the latter are somewhat different than what was previously reported.

ICP analyses indicate that the Ca and Cu contents are slightly lower than the nominal compositions of $Ca_2Mn_3O_8$ and $Cu_2Mn_3O_8$ would indicate. This implies that the oxygen content is correspondingly lower as well (i.e., there are fewer transition metal vacancies than expected). The redox titrations give Mn oxidation states of +4 for M=Cu and +3.95 for M=Ca, allowing the oxygen contents to be determined. The actual compositions determined from the ICP and redox titration results are also listed in Table 1, but for reasons of simplicity, the nominal compositions will be used to refer to these compounds throughout this paper.

Attempts to ion exchange $Ca_2Mn_3O_8$ by refluxing the powder in excess LiBr in hexanol did not succeed, resulting only in a slight reduction of the compound. This suggests, not surprisingly, that the Ca^{2+} ions in the interlayer gaps have limited mobility. Exposing $Ca_2Mn_3O_8$ powders to molten lithium nitrate for a prolonged period, however,

resulted in nearly complete conversion to a layered lithiated manganese oxide with R3m or O3 symmetry (Figure 4 and Table 1). Several weak reflections in the powder pattern can be assigned to $Ca_2Mn_3O_8$, but the elemental analyses indicate that over 95% of the calcium was replaced by lithium. The reflections of the main compound are very broad, suggesting disorder and/or very small particle size. BET analysis gives a surface area of about 50-55 M^2/g, similar to that of the parent compound. This suggests a loss of crystallinity, rather than particle breakdown, as the source for the peak broadening.

A simple exchange of two Li^+ ions for each Ca^{2+} ion should give the compound "$Li_4Mn_3O_8$". Because Li^+ ions are smaller than Ca^{2+}, they would most likely occupy all the available octahedral sites between the $Mn_3O_8^{4-}$ layers rather than the trigonal prismatic sites that are occupied by Ca^{2+} in the parent compound. This is somewhat analogous to the ion-exchange processes of P2 or P3-Na_xMnO_2 materials, which are converted to lithiated O2 or O3 analogs [1]; i.e., lithium in octahedral sites replaces the original sodium in trigonal bipyramidal sites and induces a shift of some of the transition metal layers.

The results of the elemental analysis and redox titration on the lithiated product, however, indicate that the reaction was more complex than a simple ion exchange. The Li:Mn ratio is much lower than the predicted 4:3. The redox titration also indicates that Mn oxidation state is +3.75, not close to +4 as in the parent compound. These facts indicate that both Li (most likely in the form of Li_2O) and oxygen was lost during processing. This is not too surprising, because the molten salt environment at elevated temperatures is extremely harsh; in fact, it is somewhat surprising that spinel conversion did not occur under these conditions. This structure is undoubtedly highly disordered; the

formula suggests that some Li may be located in Mn sites and vice versa. At any rate, the ordered vacancies depicted in Figure 1a are not likely to have been retained. Additionally, the octahedral sites in the lithium layer are not fully occupied, as is the case with the O3 lithiated analogs to P3 sodium-containing layered manganese oxide phases [2, 3].

It is interesting that the lithiated material is rhombohedral, consistent with an average oxidation state of Mn above +3.5. Below this value, the large number of Mn^{3+} ions causes a cooperative Jahn-Teller distortion that reduces the symmetry of O3 layered compounds to monoclinic, as with $LiMnO_2$ prepared from α-$NaMnO_2$ [13]. In $Ca_2Mn_3O_8$ and $Cu_2Mn_3O_8$, the stacking arrangement of the alternating Mn-containing and M^{2+}-containing layers result in a reduced symmetry (not all $M_2Mn_3O_8$ compounds are monoclinic; e.g., $Co_2Mn_3O_8$ which has Co in both tetrahedral and octahedral sites is orthorhombic [4]). Thus, the product of the molten salt reaction can be considered to bear a structural relationship to the hypothetical $Li_4Mn_3O_8$ although it is not identical and is compositionally different.

Electrochemical Characterization

Figure 5 shows the first discharge profiles of $Ca_2Mn_3O_8$ and $Cu_2Mn_3O_8$ in lithium cells at low discharge currents. For the Li/$Ca_2Mn_3O_8$ cell in this Figure, the profile is sloping and reaches 1V vs. Li when current equivalent to 2 Li^+/$Ca_2Mn_3O_8$ is passed. Although lithium may be inserted into 2d sites in the transition metal layers (vacancies) with concomitant reduction of Mn, this accounts for only 1 Li^+/$Ca_2Mn_3O_8$ at the maximum. Any additional Li^+ must be intercalated into the Ca^{2+}-containing layers. To do

this must require partial or full displacement of Ca^{2+} ions, which otherwise would be unreasonably close to the added Li^+ ions in the van der Waal's gaps.

The shapes of the voltage curves for $Li/Ca_2Mn_3O_8$ cells differ depending upon the discharge conditions; they are flatter when cells are stepped potentiostatically at lower overall C rates, for example. It is very difficult to exceed the composition of about $2Li^+/Ca_2Mn_3O_8$ whether cells are discharged potentiostatically or galvanostatically. These observations imply that there are severe kinetic limitations to the redox processes, and that the system is not close to equilibrium even when discharged or stepped potentiostatically at extremely low rates. Interestingly, shallow cycling is possible suggesting partial reversibility, although the charge curves do not have the same shapes as the discharge profiles (not shown).

An *ex situ* XRD experiment, in which two different $Li/Ca_2Mn_3O_8$ cells were discharged, allowed to rest, and taken apart at points A and B, respectively (Figure 6a) was carried out. The second cell was driven past 2 $Li^+/Ca_2Mn_3O_8$ by stopping and starting the current repeatedly. The XRD patterns of the discharged electrodes (Figure 6b) show evidence of the formation of a new phase, marked by arrows. For the electrode discharged to point B (3.6 $Li^+/Ca_2Mn_3O_8$), reflections due to the original phase are weak and broad, indicating that most of it has been destroyed and replaced with the new phase. The electrode discharged to point A (1.3 $Li^+/Ca_2Mn_3O_8$) still has distinct reflections assignable to $Ca_2Mn_3O_8$, and appears to be a phase mixture.

$Li/Cu_2Mn_3O_8$ cells exhibit quite different electrochemical behavior (Figure 5). The discharge profile consists of three regions; a steeply sloping portion to about 0.2 $Li^+/Cu_2Mn_3O_8$, followed by a long plateau at 1.5V to about 4 $Li^+/Cu_2Mn_3O_8$, and finally a

gently sloping region between 4 and 7 Li^+/ $Cu_2Mn_3O_8$ to 1V. The discharge processes appear to be much less kinetically limited than those of $Ca_2Mn_3O_8$, and slow potentiostatic experiments are reasonably consistent with faster galvanostatic ones. Some discharge profiles, however, show a slight rise and then fall in potential in the region between 0.2 and 4 $Li^+/Cu_2Mn_3O_8$, depending upon the current density used. Cells are only partly rechargeable depending upon the voltage limits chosen.

The results of *ex situ* XRD experiments are shown in Figure 7a and b. Electrodes from a fresh cell (point A) and those from two cells discharged to points B and C, as well as one discharged and then charged to point D were examined. The XRD patterns of the cycled electrodes show a new phase growing in, whose reflections are marked with arrows. At point C (3.3 $Li^+/Cu_2Mn_3O_8$), peaks due to the original $Cu_2Mn_3O_8$ are still apparent, although less so than in the electrode stopped at point B. After deep discharge and partial recharge (point D), most of the original electrode material is gone and has been replaced with the new phase. A comparison of Figures 6 and 7 indicates that the new material formed upon discharge of $Li/Ca_2Mn_3O_8$ cells is identical to that in $Li/Cu_2Mn_3O_8$ ones. A new strong low angle reflection at $2\theta=17.1°$ is clearly evident in the cycled $Cu_2Mn_3O_8$ electrodes (it is less obvious in the $Ca_2Mn_3O_8$ ones, because it coincides almost exactly with the 200 peak of the parent compound), implying that this compound is a layered lithium manganese oxide, possibly $Li_4Mn_3O_8$ or a related material. The presence of several small reflections near $2\theta=50°$ indicates that the symmetry is lower than rhombohedral (compare Figure 4), although it is not possible to assign a structure definitively at this time.

The presence of this phase in $Cu_2Mn_3O_8$ cells implies that Cu^{2+} ions are displaced from the interlayers. At the operating potential of the Li/$Cu_2Mn_3O_8$ cells, these ions should spontaneously be reduced to metallic Cu. Unfortunately, peaks in the XRD patterns due to Cu (or Cu_2O) are expected to coincide exactly with reflections due to other phases and components in the $Cu_2Mn_3O_8$ electrodes, making it impossible to detect these materials. However, evidence of copper redox processes can be seen in the cycling profile of a Li/$Cu_2Mn_3O_8$ cell in which the first discharge is limited to ~4 $Li^+/Cu_2Mn_3O_8$ (Figure 8a). Almost no charge can be passed until the cell voltage reaches about 3.4 V, as would be expected if $Li_4Mn_3O_8$ and metallic copper are formed during discharge. Above this potential, approximately half the original capacity is recovered, although the electrochemical processes are clearly different from those upon discharge. The differential capacity plot shows a sharp peak at 3.44 V (Figure 8b) consistent with oxidation of Cu^0 to Cu^+. The subsequent discharge and charge look quite different from the first and no signature due to Cu^+ reduction is apparent; Cu^+ may instead be inserted into the $Li_4Mn_3O_8$ phase that remains from the original discharge. Ion exchange between Cu^+ and Li^+ in the electrolytic solution may also occur. The production of Cu^+ at high cell potentials complicates the electrochemical processes enormously and reproducible results can only be obtained if the charge is limited so as to prevent oxidation of Cu^0.

Once $Cu_2Mn_3O_8$ is fully converted to $Li_4Mn_3O_8$ through deep discharge, it can be cycled at low potentials with good reversibility (Figure 9a and b). The voltage profile is sloping with most of the capacity well below 2.9V vs. Li, where layered manganese oxides normally discharge. Intercalation of Li^+ into interlayer octahedral sites normally occurs at this potential, but in $Li_4Mn_3O_8$, these sites are already completely filled. There

are also two tetrahedral interlayer sites for every octahedral one, although both sets cannot both be occupied simultaneously. Johnson et al. [14] have observed low voltage capacity in layered $LiMn_{0.5}Ni_{0.5}O_2$•$(1-x)Li_2TiO_3$ electrodes, which they attribute to filling of the tetrahedral interlayer sites and concomitant reduction of Mn^{4+}. (These materials are similar to $Li_4Mn_3O_8$ in that Mn is in the +4 oxidation state in the fully lithiated state). Complete reduction of all of the Mn to +3 requires that 7/8 of the tetrahedral sites be filled with Li for a composition of $Li_7Mn_3O_8$, as is observed at the endpoint of $Li/Cu_2Mn_3O_8$ cell discharges. Further reduction of Mn below an average oxidation state of +3 and complete filling may be possible and would give $Li_8Mn_3O_8$, although it is not clear whether this would be completely reversible or not.

The lithiated compound that is formed during the molten salt reaction with $Ca_2Mn_3O_8$ shows electrochemical characteristics typical of a non-stoichiometric layered lithium manganese oxide with the average Mn oxidation state less than +4. $Li/Ca_{0.13}Li_{2.64}Mn_3O_{7.07}$ cells can be either charged or discharged initially from the starting open circuit potential of 3.3 V (Figure 10) and show the characteristic capacity near 2.9 V, consistent with insertion of Li into 3b sites. If charged initially, the capacity is consistent with complete oxidation of all Mn to the +4 state. The cells also show capacities at low potentials, reminiscent of what is seen during insertion of Li^+ into the electrochemically generated $Li_4Mn_3O_8$.

The capacity between 2.0 and 4.3V is only about 120 mAh/g (Figure 11). This is low in comparison to many other O3 layered manganese oxides [2, 3], but is consistent with defects in the transition metal layers, which effectively prevent all of the lithium from being extracted during charge limiting the capacity upon subsequent discharge. As

is typical of the O3 compounds, capacity near 4V develops upon cycling (inset in Figure 4), indicative of a slow phase conversion into spinel. The oxygen array in O3 and spinel structures is nearly the same, requiring only rearrangement of cations. This occurs readily if Mn^{3+} ions and vacancies in the lithium layer co-exist during electrochemical cycling [15]. $Li_4Mn_3O_8$ is rather interesting, in that this situation does not occur, and, therefore, spinel conversion should not happen.

The electrochemical processes in $Ca_2Mn_3O_8$ and $Cu_2Mn_3O_8$ cells undergoing discharge are clearly quite complex. The observations outlined above are consistent with the following reactions on the positive electrode side for $Li/Cu_2Mn_3O_8$ cells:

$$Cu_2Mn_3O_8 + x\ Li^+ + x\ e^- \rightarrow Li_xCu_2Mn_3O_8 \quad (x \text{ very small}) \qquad (1)$$

$$Li_xCu_2Mn_3O_8 \rightarrow 1/4x\ Li_4Mn_3O_8 + 3/4x\ Cu_2Mn_3O_8 + 1/2x\ Cu^0 \qquad (2)$$

$$Li_4Mn_3O_8 + yLi^+ + ye^- \rightarrow Li_{4+y}Mn_3O_8\ (y \leq 3\text{-}4) \qquad (3)$$

Reductive intercalation (step 1), with Li^+ most likely inserting into the 2d sites in the $Mn_3O_8^{4-}$ sheets, happens during the initial sloping part of the discharge. Very little is intercalated before the phase separation shown in step 2 occurs. This produces $Li_4Mn_3O_8$ and regenerates the starting material, which can then undergo further reduction via step 1 and phase separation via step 2 until it is totally consumed or the current is shut off. The overall effect is that of an electrochemically-induced ion exchange; simple ion exchange with the electrolytic solution is not likely to be significant. Once $Li_4Mn_3O_8$ is formed, it, too, can undergo reductive intercalation (step 3), which is a reversible process. Interestingly, it is first produced below the potential at which it is stable, so that it

spontaneously reduces, leading to the observed inflections in some of the discharge profiles (e.g., in Figure 8a).

The precipitation of Cu metal drives the electrochemically-induced ion exchange forward and makes the discharge processes in $Cu_2Mn_3O_8$ electrodes occur fairly rapidly (it may also help by improving the electronic conductivity of the electrode as the reactions progress). In contrast, Ca^{2+} ions displaced by Li^+ ions are not reduced at the discharge potentials of $Li/Ca_2Mn_3O_8$ cells (until they migrate to the negative electrode, where calcium metal may plate). The mechanism of discharge probably differs somewhat for $Ca_2Mn_3O_8$ than for $Cu_2Mn_3O_8$; at any rate, it is much less facile. The implied release of Ca^{2+} ions into the electrolytic solution and the sluggishness of the electrochemical reactions make $Ca_2Mn_3O_8$ impractical for use in lithium cells.

The electrochemical characteristics of these electrodes are of interest mainly because they demonstrate that M^{2+} cations are mobile at room temperature under certain circumstances. For example, attempts to stabilize layered manganese oxides against spinel formation by pillaring the layers with M^{2+} cations are unlikely to be successful if the cations can be readily displaced during discharge. Cu^{2+}, in particular, would be a bad choice for such a role. Additionally, redox systems employing $M^{2+} \leftrightarrow M^0$ couples (e.g., especially M=Mg), are of interest for next-generation batteries [16]. Because of the low mobility of M^{2+} ions, the choice of cathode material is extremely restricted [17]. The fact that Cu^{2+} can be readily displaced from between $Mn_3O_8^{4-}$ sheets suggests that it may be fruitful to explore conventional layered materials, particularly those with vacancies in the transition metal sheets, as possible intercalation compounds for these batteries.

Conclusions

A layered lithium manganese oxide, probably $Li_4Mn_3O_8$, forms during discharge of Li/$Ca_2Mn_3O_8$ and Li/$Cu_2Mn_3O_8$ cells, indicating that the M^{2+} (Ca^{2+} or Cu^{2+}) ions are displaced from the positive electrode structures. The electrochemical processes are very slow for $Ca_2Mn_3O_8$, however, and the reaction does not go to completion. In the case of $Cu_2Mn_3O_8$, precipitation of metallic Cu during the reduction drives the reaction forward, and electrodes can be discharged easily, although the reduction processes are only partially reversible. Once $Li_4Mn_3O_8$ is formed from $Cu_2Mn_3O_8$ electrodes, it can undergo further Li intercalation to form $Li_7Mn_3O_8$, reversibly. A layered lithium manganese oxide is also produced when $Ca_2Mn_3O_8$ is reacted with molten lithium nitrate. The process is not a simple ion-exchange, resulting in an O3 layered material structurally related to $Li_4Mn_3O_8$ but with fewer transition metal vacancies. This material exhibits electrochemical behavior similar to O3 layered manganese oxides made from sodium-containing precursors.

Acknowledgments

This work was supported by the Assistant Secretary for Energy Efficiency and Renewable Energy, Office of FreedomCAR and Vehicle Technologies of the U.S. Department of Energy under contract no. DE-AC02-05CH11231. This work was also supported by the Korea Research Foundation Grant (M01-2004-000-20008-0) (YJP). We would like to thank Dr. Kwang Sun Ryu for helpful discussion.

References

1. T. A. Eriksson, Y. J. Lee, J. Hollingsworth, J. A. Reimer, E.J. Cairns, X.-F. Zhang, and M. M. Doeff, Chem. Mater. 15 (2003) 4456-4463.

2. M. Dollé, S. Patoux, and M. M. Doeff, Chem. Mater. 17 (2005) 1036-1043.

3. S. Patoux, M. Dollé, and M. M. Doeff, Chem. Mater. 17 (2005) 1044-1054.

4. A. Riou and A. Lecerf, Acta Cryst. B31 (1975) 2487-2490.

5. H.R. Oswald and M.J. Wampetich, Helv. Chim. Acta 50 (1967) 2023-2034.

6. A. Lecerf, C.R. Acad. Sc. Paris, Sér. C 279 (1974) 879-882.

7. A. Riou and A. Lecerf, Acta Cryst. B33 (1977) 1896-1900.

8. G. B. Ansell, M. A. Modrick, J. M. Longo, K.R. Poeppelmeyer, and H.S. Horowitz, Acta Cryst. B38 (1982) 1795-1797.

9. J.-P. Parant, R. Olazcuaga, M. Devalette, C. Fouassier, and P. Hagenmuller, J. Sol. State Chem. 3 (1971) 1-11.

10. M. Morcrette, P. Rozier, L. Dupont, E. Mugnier, L. Sannier, J. Galy, and J.-M. Tarascon, Nat. Mater. 2 (2003) 755-761.

11. A. Lecerf, C.R. Acad. Sc. Paris Sér. C 277 (1973) 969-971.

12. M. J. Katz, R. C. Clarke, and W.F. Nye, Anal. Chem. 28 (1956) 507-508.

13. A. D. Robertson, A. R. Armstrong, and P. G. Bruce, Chem. Mater. 13 (2001) 2380-2386.

14. C. S. Johnson, J.-S. Kim, A. J. Kropf, A. J. Kahaian, J. T. Vaughey, and M. M. Thackeray, Electrochem. Commun. 4 (2002) 492-498.

15 J. Reed and G. Ceder, Chem. Rev. 104 (2004) 4513-4534.

16. D. Aurbach, Z. Lu, A. Schechter, Y. Gofer, H. Gizbar, R. Turgeman, Y. Che, M. Moshkovich, and E. Levi, Nature 407 (2000) 724-727.

17. P. Novák, R. Imhof, and O. Haas, Electrochim. Acta 45 (1999) 351-367.

Table 1. Composition and Structural Parameters of $M_2Mn_3O_8$ (M=Ca, Cu) and derivatives.

Nominal composition	Actual composition[a]	Space group	Lattice Parameters			
			a, Å	b, Å	c, Å	β
$Cu_2Mn_3O_8$	$Cu_{1.89}Mn_3O_{7.89}$	C/2m	9.645	5.6385	4.913	101.2°
$Ca_2Mn_3O_8$	$Ca_{1.78}Mn_3O_{7.69}$	C/2m	11.017	5.8295	4.939	109.7°
Li exchange[b]	$Ca_{0.13}Li_{2.64}Mn_3O_{7.07}$	$R\bar{3}m$	2.844	—	14.365	—

a) determined by ICP and redox titration.

b) product of molten $LiNO_3$ exchange of $Ca_2Mn_3O_8$.

Figure Captions

Figure 1. (a) A single $Mn_3O_8^{4-}$ sheet. (b) Structure of $Cu_2Mn_3O_8$, showing Cu^{2+} ions in square pyramids between $Mn_3O_8^{4-}$ layers. (c) Structure of $Ca_2Mn_3O_8$, showing Ca^{2+} in trigonal bipyramids between $Mn_3O_8^{4-}$ layers.

Figure 2. Calculated (bottom) and experimental (top) XRD patterns of $Cu_2Mn_3O_8$. Al from the sample holder is indicated and major reflections are identified.

Figure 3. Calculated (bottom) and experimental (top) XRD patterns of $Ca_2Mn_3O_8$. Al from the sample holder is indicated and major reflections are identified.

Figure 4. Calculated (bottom) and experimental (top) XRD patterns of the product of the ion-exchange of $Ca_2Mn_3O_8$ (=$Ca_{0.13}Li_{2.64}Mn_3O_{7.07}$). Major reflections are identified. Reflections assigned to $Ca_2Mn_3O_8$ are marked with an *.

Figure 5. Discharge profiles of Li/$Ca_2Mn_3O_8$ and Li/$Cu_2Mn_3O_8$ cells discharged at 0.011 mA/cm^2.

Figure 6. Discharge profile (left) of Li/$Ca_2Mn_3O_8$ cells, showing points at which cells were disassembled and cathodes were subjected to *ex situ* XRD analysis (right). Peaks attributable to a new phase are marked with arrows, and reflections due to cell components are marked G (for graphite) or Al. The current density used to discharge the

cells was 0.011 mA/cm^2. Beyond approximately 2 Li/$Ca_2Mn_3O_8$, the current was stopped and started periodically to allow deeper discharge.

Figure 7. Cycling profile (left) of Li/$Cu_2Mn_3O_8$ cells, showing points at which cells were disassembled and cathodes were subjected to *ex situ* XRD analysis (right). Peaks attributable to a new phase are marked with arrows, and reflections due to cell components are marked G (for graphite) or Al. The current density used to discharge the cells was 0.011 mA/cm^2.

Figure 8. Galvanostatic cycling (left) of a Li/$Cu_2Mn_3O_8$ cell at 0.0055 mA/cm^2 and differential capacity plot of the first cycle (right) obtained by taking the derivative of the voltage profile.

Figure 9. One complete discharge and charge of a Li/$Cu_2Mn_3O_8$ cell at 0.011 mA/cm^2 after complete conversion to $Li_4Mn_3O_8$ (left), and the first and fifth discharges after conversion at the same rate (right).

Figure 10. The first discharge and subsequent full cycle of a Li/ $Ca_{0.13}Li_{2.64}Mn_3O_{7.07}$ cell at 0.027 mA/cm^2 between 1.2 and 4.3V.

Figure 11. 1st and 25th discharges at 0.027 mA/cm^2 between 4.3 and 2.0 V of a Li/ $Ca_{0.13}Li_{2.64}Mn_3O_{7.07}$ cell. Inset shows the differential capacity plot in the 4V region.

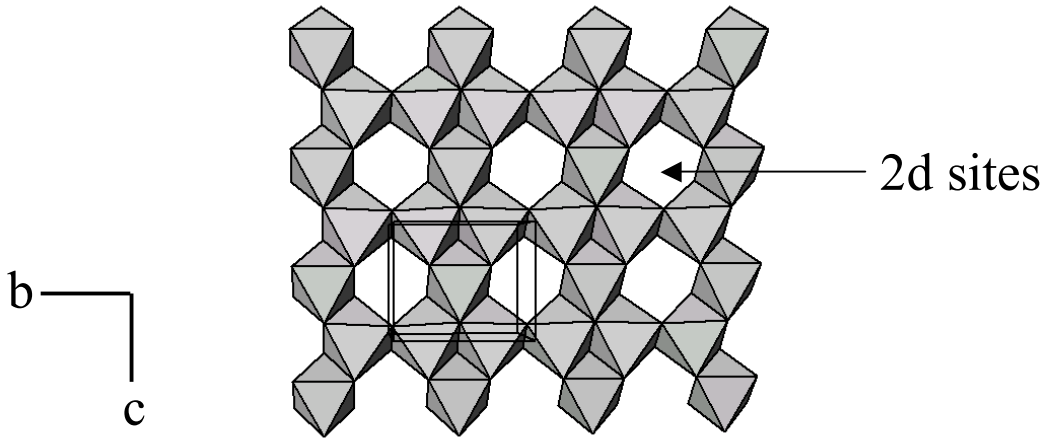

(a)

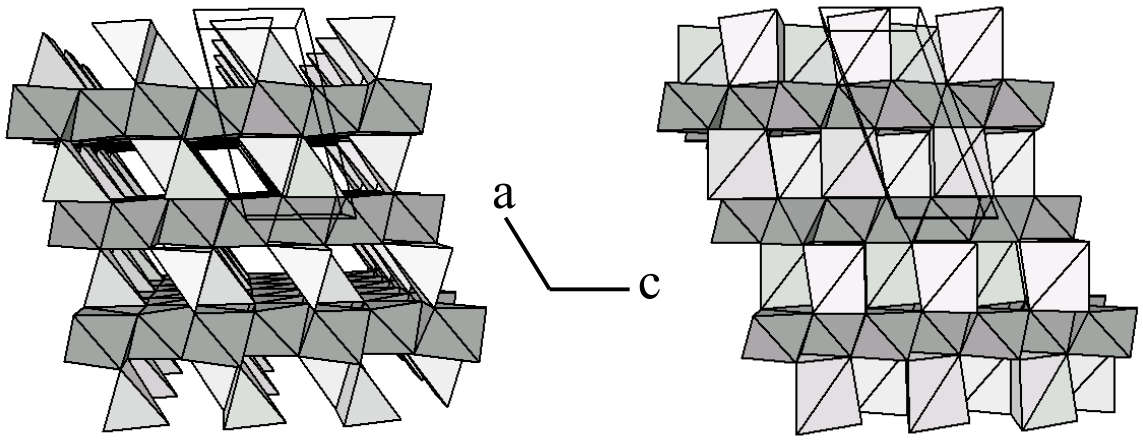

(b) (c)

Figure 1.

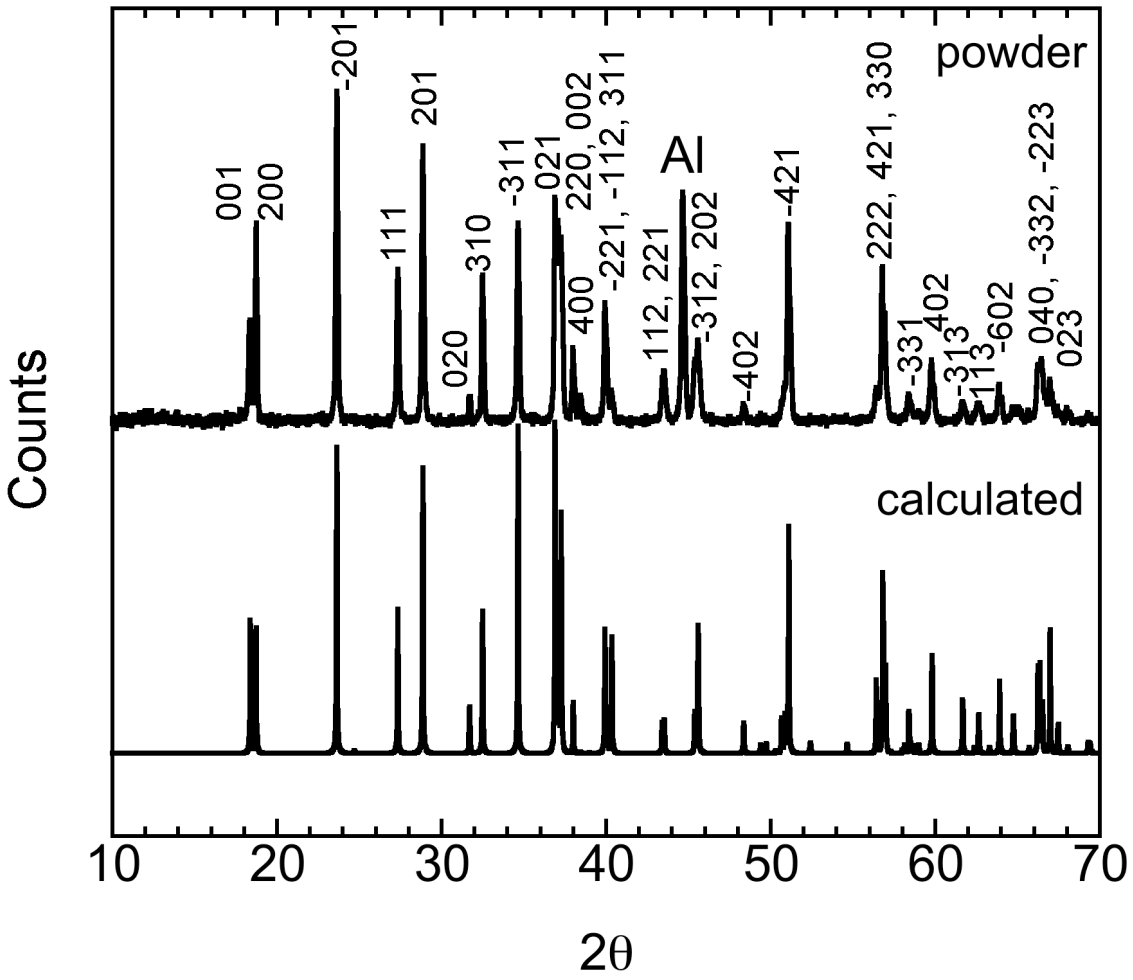
powder
calculated
Al
Counts
2θ
10
20
30
40
50
60
70
001
200
-201
111
201
020
310
-311
021
220, 002
-221, -112, 311
400
112, 221
-312, 202
-402
-421
222, 421, 330
-331
402
-313
113
-602
040, -332, -223
023

Figure 2.

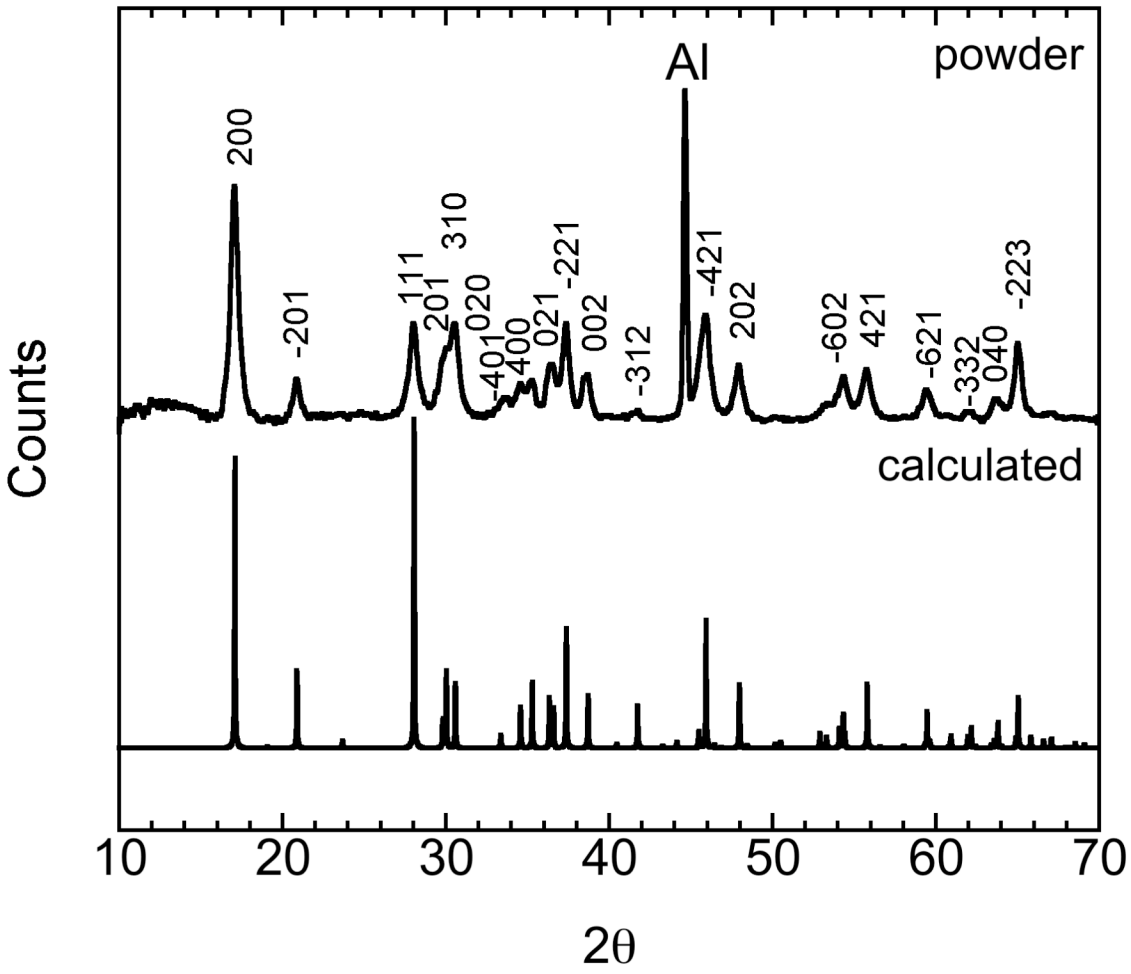
Al
powder
200
-201
111
201
310
020
-401
400
021
-221
002
-312
-421
202
-602
421
-621
-332
040
-223
calculated
Counts
10
20
30
40
50
60
70
2θ

Figure 3.

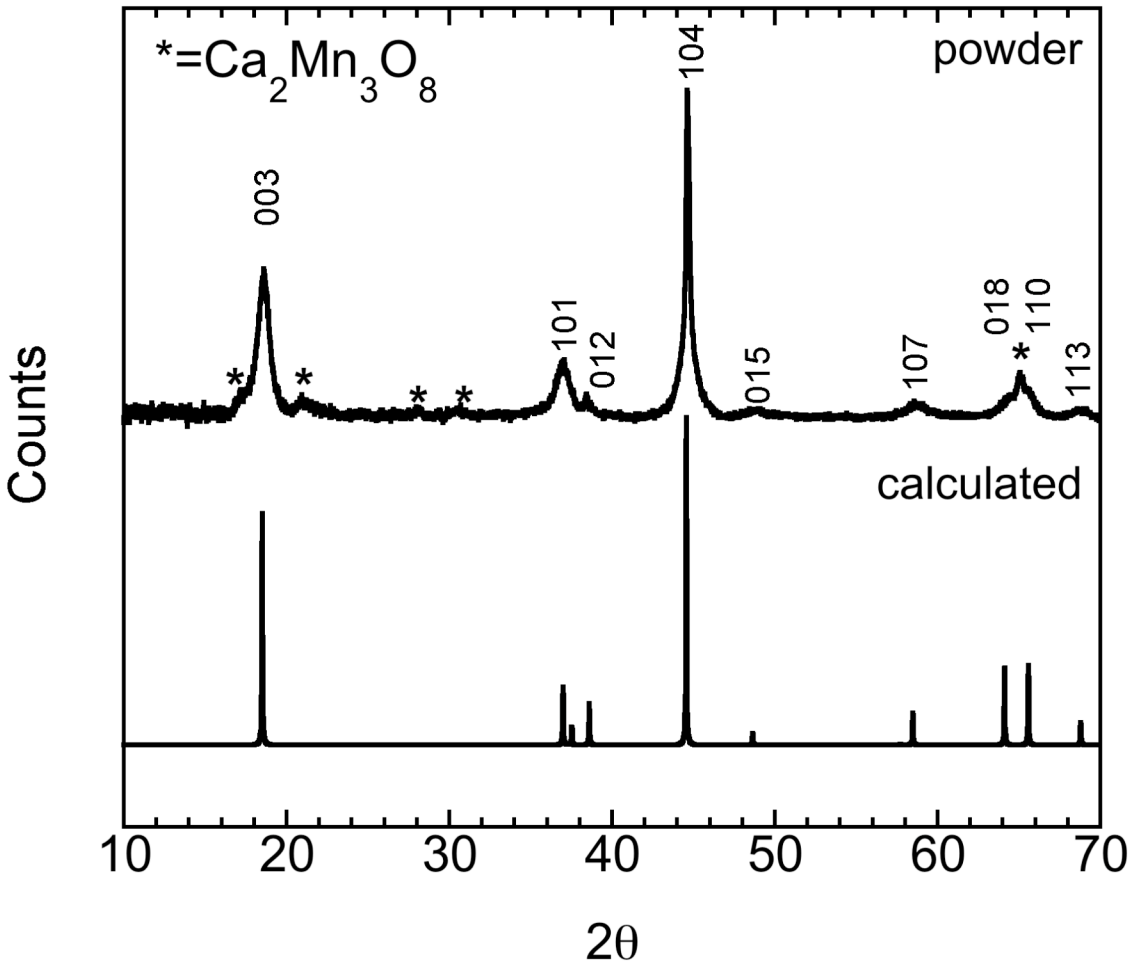
*=Ca2Mn3O8
powder
003
104
101
012
015
107
018
110
113
*
Counts
calculated
10
20
30
40
50
60
70
2θ

Figure 4.

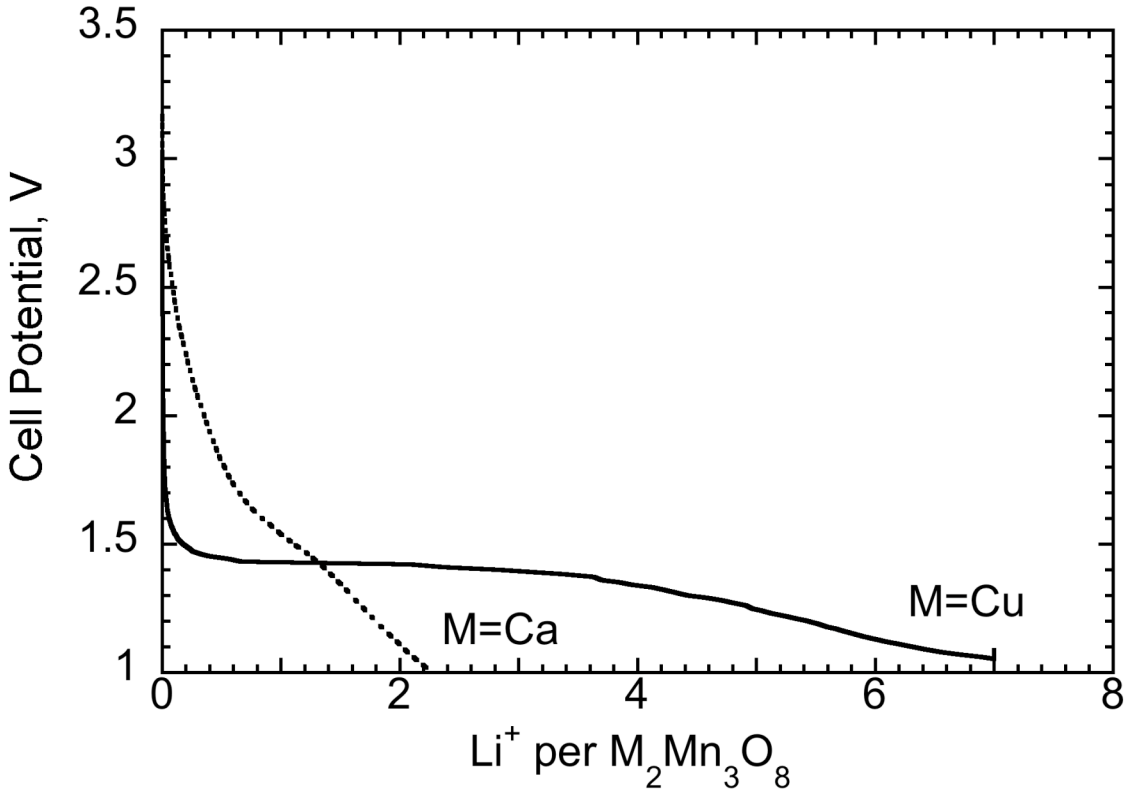

Figure 5.

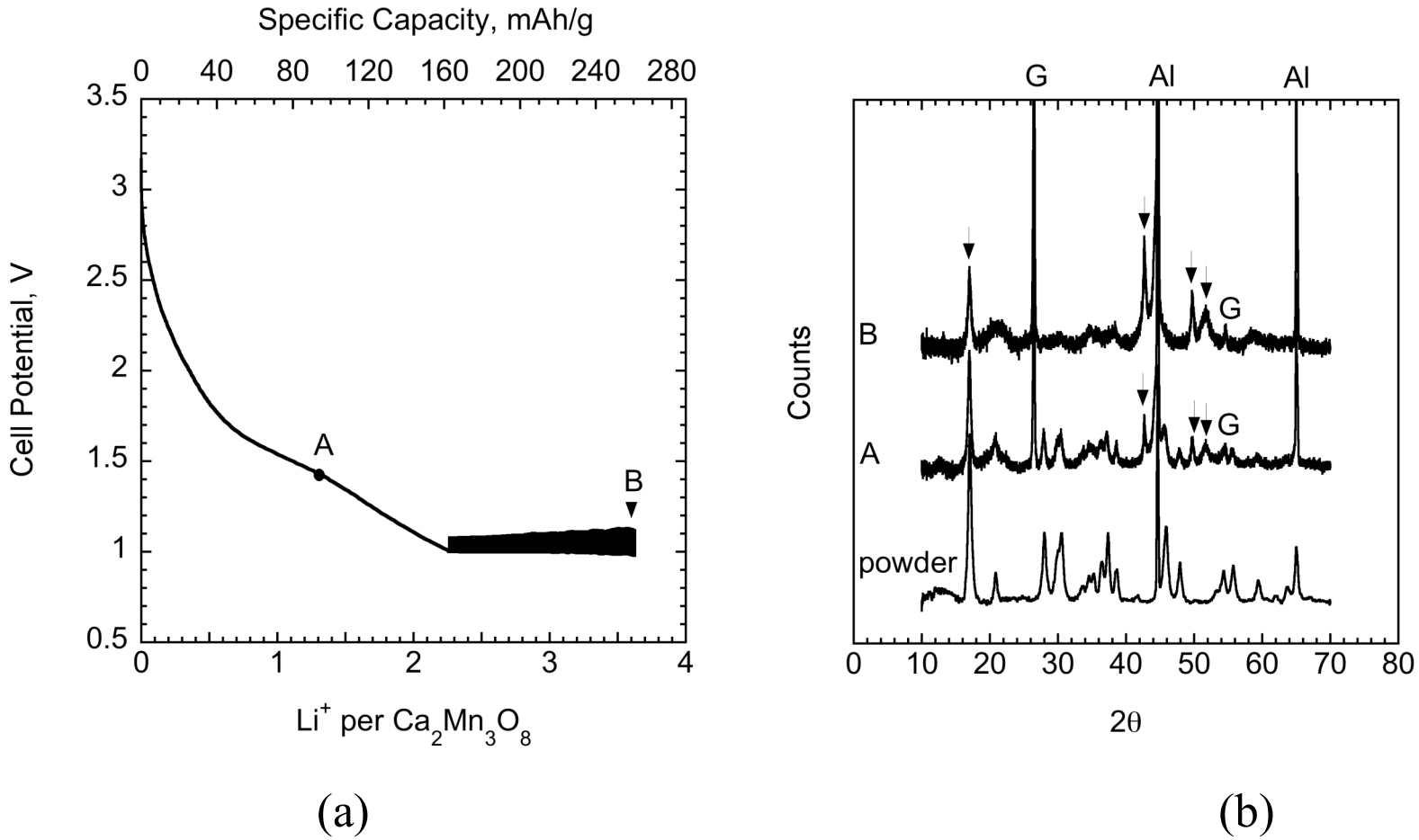
Specific Capacity, mAh/g
0
40
80
120
160
200
240
280
3.5
3
2.5
2
1.5
1
0.5
Cell Potential, V
A
B
0
1
2
3
4
Li+ per Ca2Mn3O8
(a)
G
Al
Al
Counts
B
A
powder
G
G
0
10
20
30
40
50
60
70
80
2θ
(b)

Figure 6

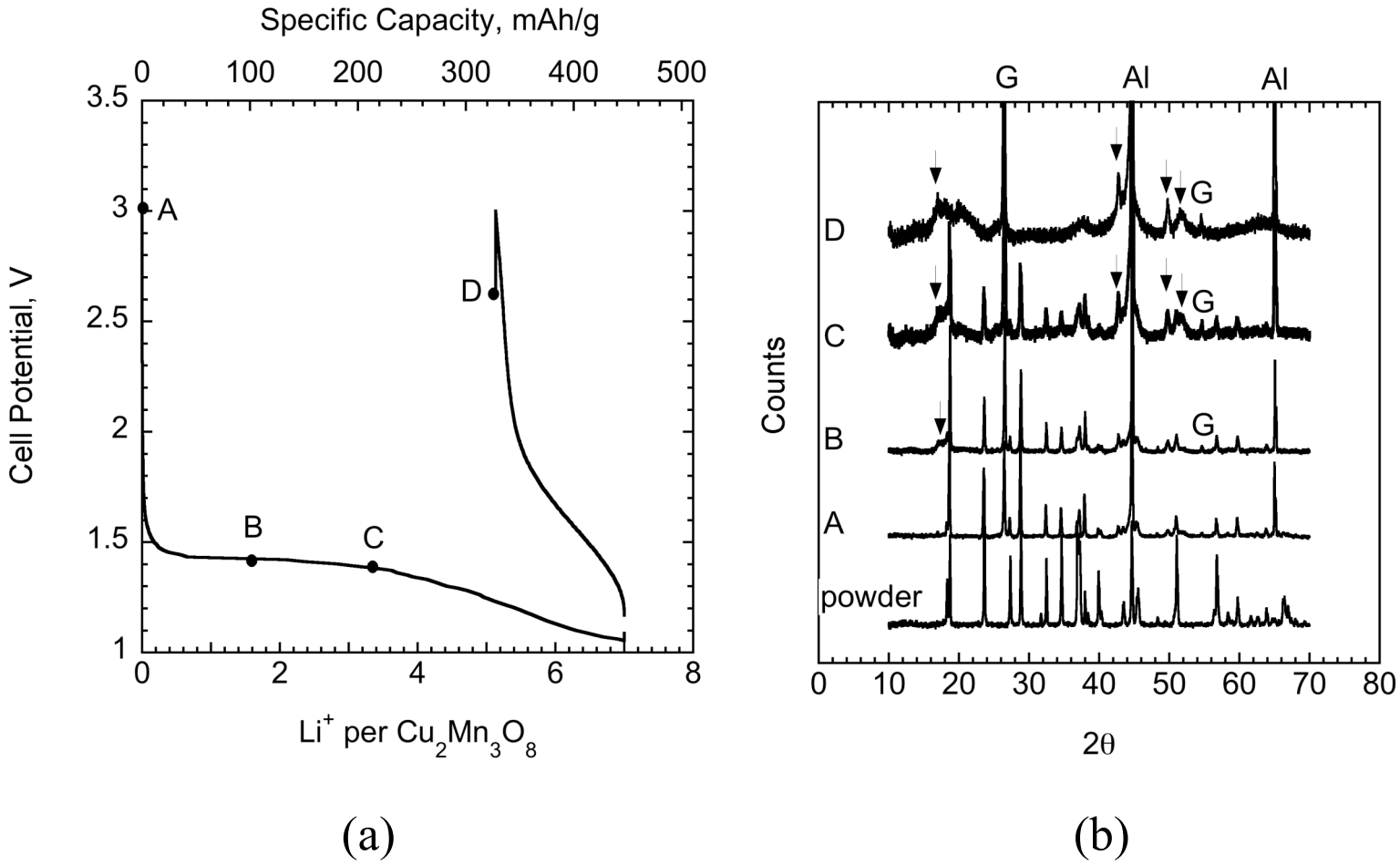
Specific Capacity, mAh/g
0
100
200
300
400
500
3.5
3
2.5
2
1.5
1
A
B
C
D
Cell Potential, V
0
2
4
6
8
Li+ per Cu2Mn3O8
(a)
G
Al
Al
G
G
G
D
C
B
A
powder
Counts
0
10
20
30
40
50
60
70
80
2θ
(b)

Figure 7.

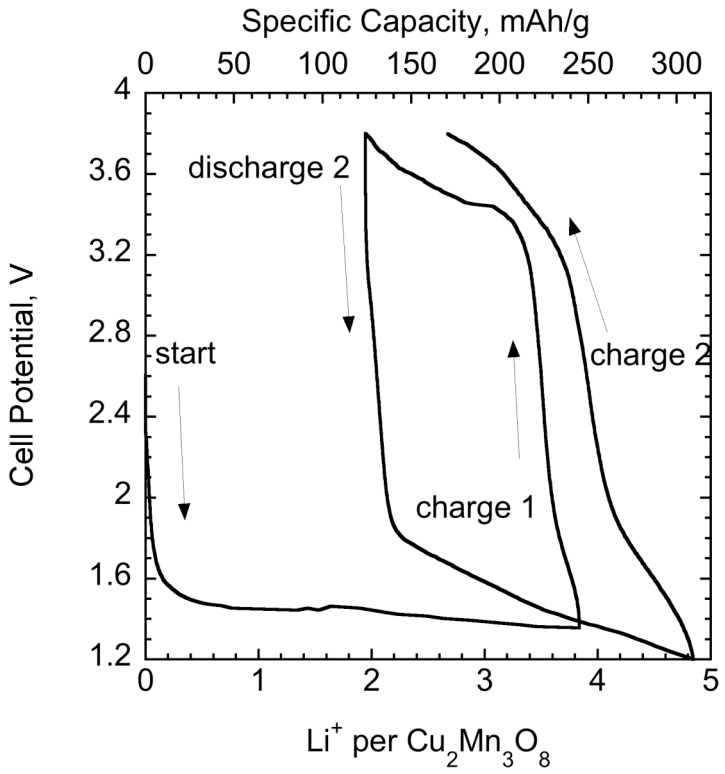
Specific Capacity, mAh/g
0
50
100
150
200
250
300
4
3.6
3.2
2.8
2.4
2
1.6
1.2
Cell Potential, V
discharge 2
start
charge 2
charge 1
0
1
2
3
4
5
Li+ per Cu2Mn3O8

(a)

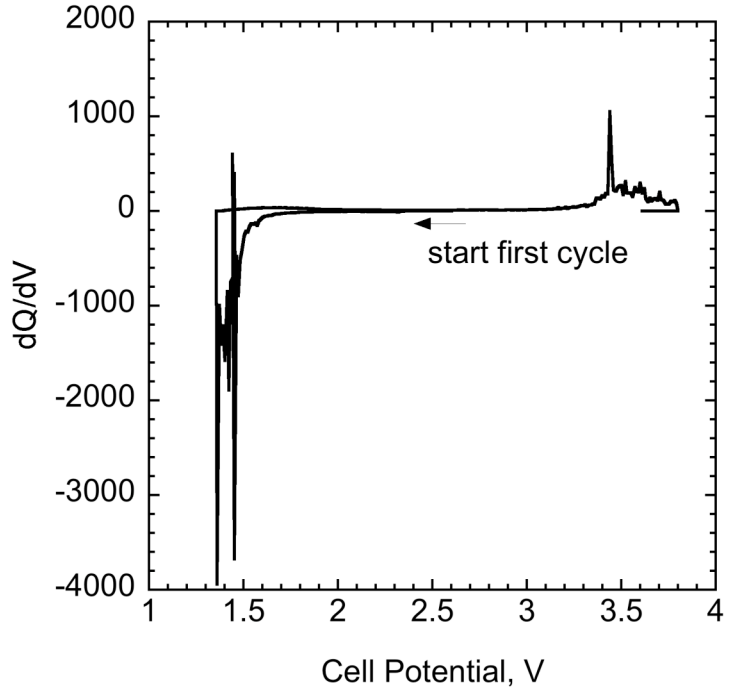
2000
1000
0
-1000
-2000
-3000
-4000
dQ/dV
start first cycle
1
1.5
2
2.5
3
3.5
4
Cell Potential, V

(b)

Figure 8.

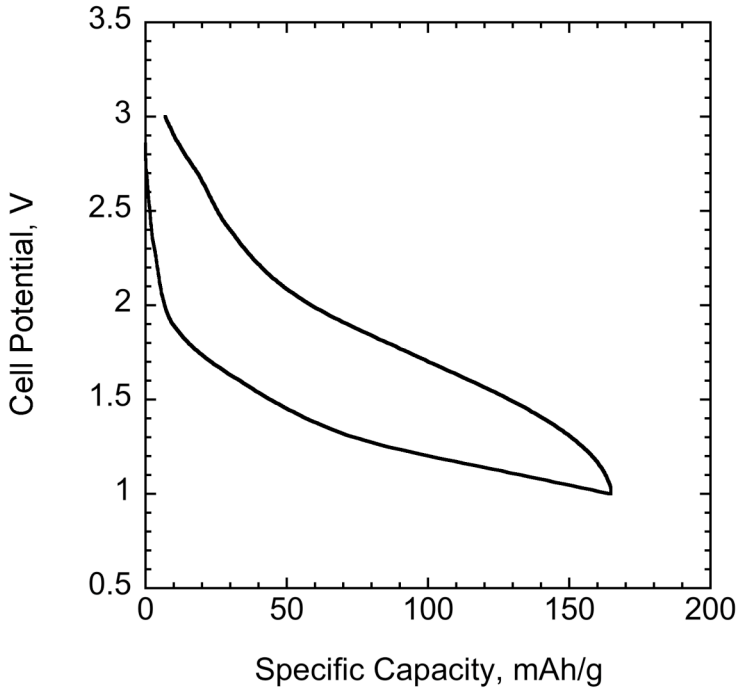
Cell Potential, V
Specific Capacity, mAh/g
3.5
3
2.5
2
1.5
1
0.5
0
50
100
150
200

(a)

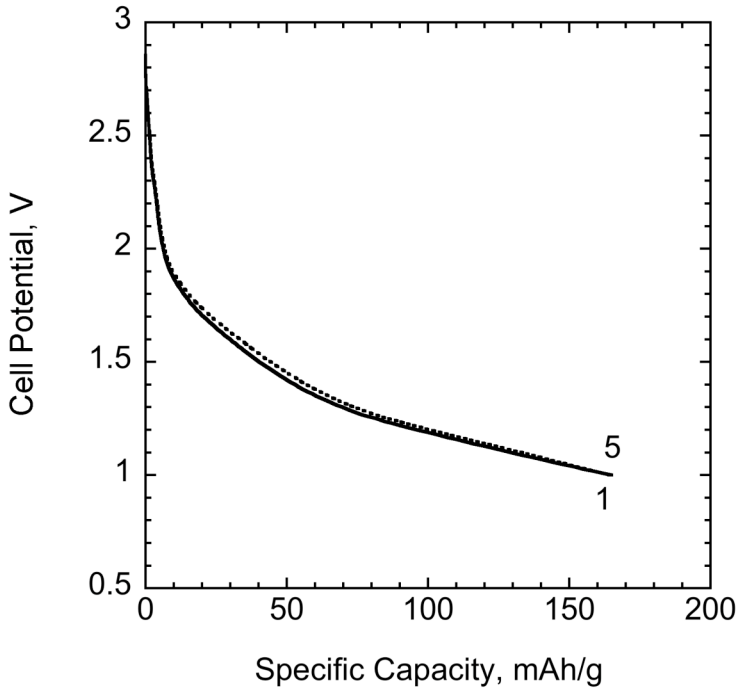
Cell Potential, V
Specific Capacity, mAh/g
3
2.5
2
1.5
1
0.5
0
50
100
150
200
5
1

(b)

Figure 9

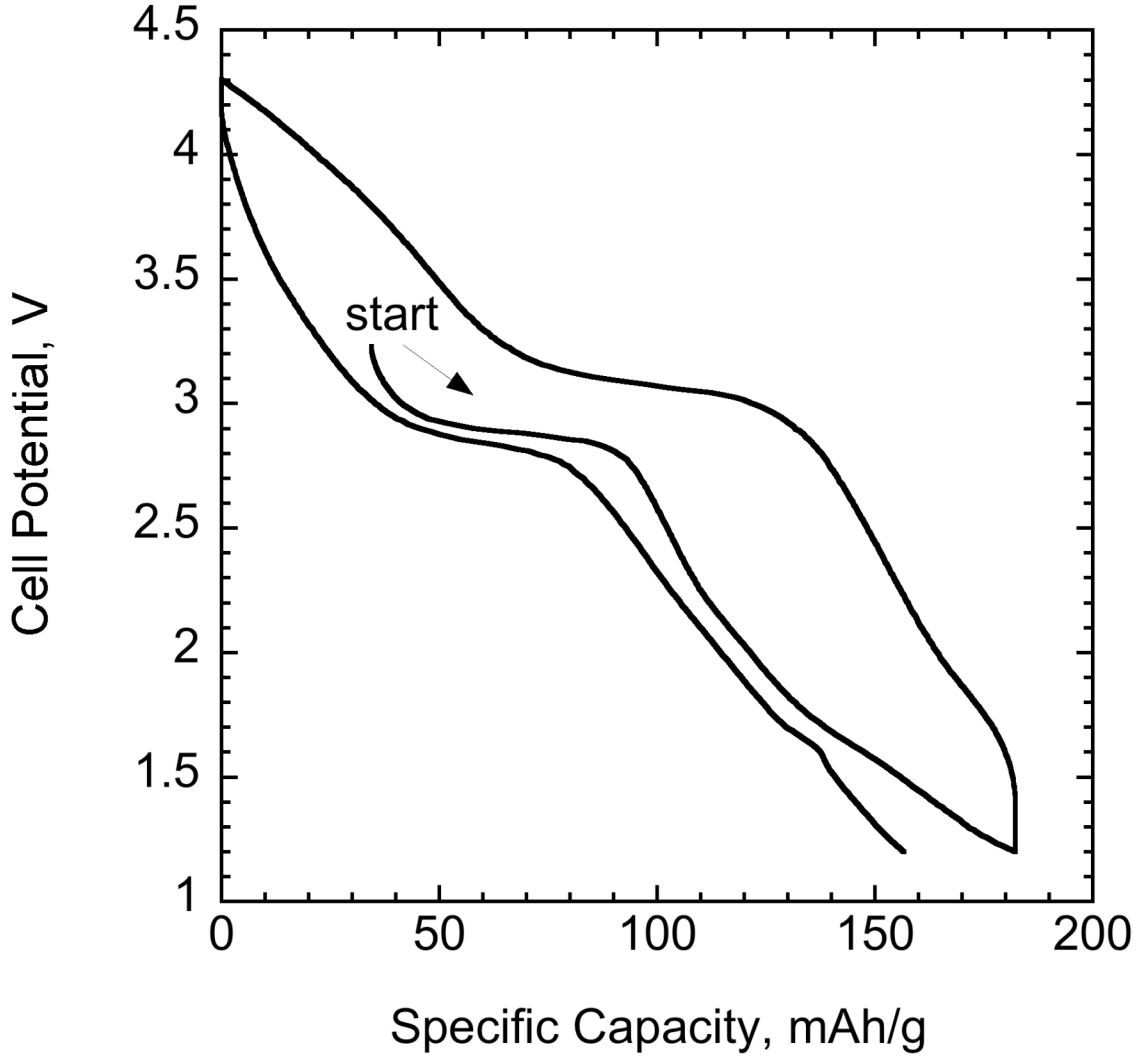
4.5
4
3.5
3
2.5
2
1.5
1
0
50
100
150
200
Cell Potential, V
Specific Capacity, mAh/g
start

Figure 10

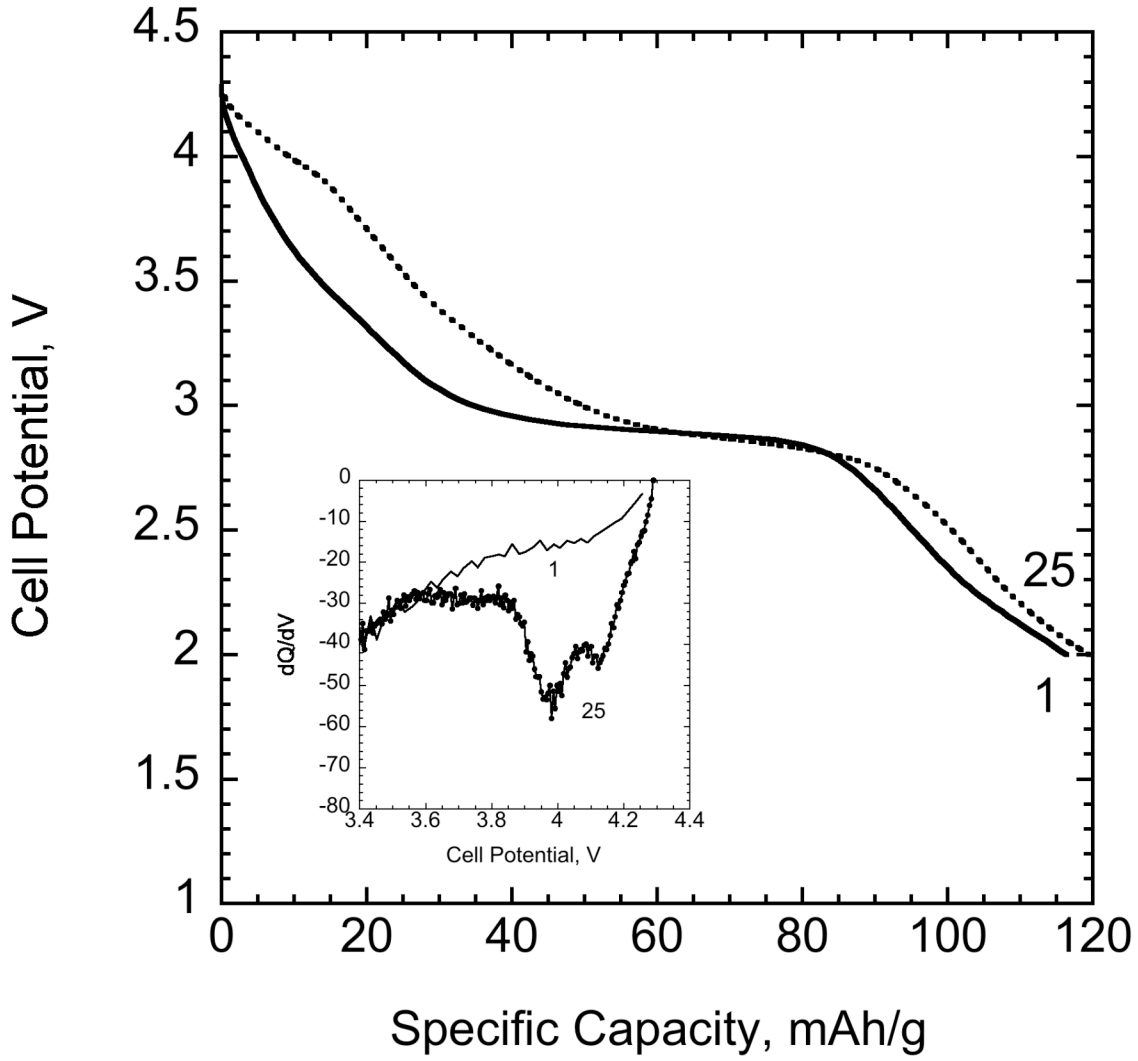
Cell Potential, V
Specific Capacity, mAh/g
4.5
4
3.5
3
2.5
2
1.5
1
0
20
40
60
80
100
120
25
1
dQ/dV
0
-10
-20
-30
-40
-50
-60
-70
-80
3.4
3.6
3.8
4
4.2
4.4
Cell Potential, V
1
25

Figure 11